공학석사학위논문

Highly Sensitive and Stretchable Multi-dimensional Strain Sensor with Pre-strained Anisotropic Metal Nanowire Percolation Networks

금속 나노와이어의 이방성 패턴을 이용한 유연
다차원 스트레인 센서 개발

2016 년 2 월

서울대학교 대학원

기계항공공학부

김 권 규

Highly Sensitive and Stretchable Multi-dimensional Strain Sensor with Pre-strained Anisotropic Metal Nanowire Percolation Networks

지도교수 고 승 환

이 논문을 공학석사 학위논문으로 제출함
2016 년 2 월

서울대학교 대학원
기계항공공학부
김 권 규

김권규의 공학석사 학위논문을 인준함
2015 년 12 월

위 원 장 _____최 만 수_____ (인)
부위원장 _____고 승 환_____ (인)
위 원 _____이 정 훈_____ (인)

Abstract

Novel designs for flexible strain-gauge sensors have been widely reported, yet remained unsuccessful in distinguishing complex characteristics of the multi-dimensional strain. Here, to overcome the limitation of the conventional single axis-strain sensor, we demonstrate a multi-dimensional strain sensor composed of two layers of pre-strained silver nanowire percolation network with decoupled and polarized electrical response in principal and perpendicular directional strain. The information on the magnitude and effective direction of surface strain are successfully calculated up to 35 % maximum strain. At the same time, the fabricated multi-dimensional sensor exhibits a markedly large gauge factor (>20) at excellent agreement with a model predicted by 3D percolation theory. The potential of the proposed sensor as a versatile wearable device has been further confirmed through its implementation as a large-area multi pixel strain sensor array on a human hand and a remote controller for an artificial 3D simulation model.

Keyword : multi-axis strain sensor, nanowire percolation network, stretchable electronics, anisotropic resistance change

Student Number : 2014-20654

Table of Contents

List of Figures

deformation in comparison with the theoretical value derived by 3D percolation theory. **(c)** Sheet resistance as a function of the volume of silver nanowires. The inset shows a logarithmic plot of the data with a linear fit.

Figure 7 | Analyzing the height of the AgNW layer.

(a) AFM image of the boundary layer (b) SEM image of laser ablated region (c) Average height profile from AFM

Figure 8 | Monte-Carlo simulation results.

(a) Percolation probability versus nanowire concentration (b) Wire distribution at 100#/500 μm^2 (c) at 200#/500 μm^2 (d) at 300#/500 μm^2 (e) at 400#/500 μm^2

Figure 9 | Detecting off-axis principal strain. (a) Schematic of the strain

(a) Schematic of the strain components applied to the strain sensor. (b) Photographs of the metal layer rotated to different angles. (c-e) Comparison of the variation in resistance of the rotated sensor with that of the sensor strained at 90°. Blue triangle lines shows the projected strain value for 90° from experiment data for each off-axis rotation.

Figure 10 | Schematic of strain components applied on the rotated strain sensor.

Figure 11 | Real-time monitoring of load-unload strain cycles at various off-axis strain angles (0°, 45°, 90°, 30°).

Figure 12 | Cyclic response of the proposed strain sensor.

(a) Response of a strain sensor under the prescribed dynamic strain profile.

(b) Long term cyclic strain response test (1000 cycles).

Figure 13 | Multi-pixel array fabrication by laser ablation.

(a) CAD model for electrodes and multi-pixel arrays (b) CAD model for multi-pixel micro electrode channel (c) Photograph of process of laser

ablation. The inset shows the microscopic image of ablated region of nanowire (d) Microscopic image of ablated metal layer region.

Figure 14 | Demonstration of applications of multi-dimensional strain sensors. (a) Control of a virtual 3D translation stage using a multi-dimensional strain sensor. (b) Photograph of a multi-pixel strain sensor array. (c) Photograph of the sensor embedded in a glove to provide hand grip motion. (d) Mapping of the strain distribution for hand grip motion in (c). (e) FEA simulation of 45° elongation and a strain distribution of ε_x. (f) Experimental mapping of the ε_x strain distribution for random directions of strain loading. Experimental results show good agreement with FEA simulation in (e).

Chapter 1. Introduction

1.1. Study Background

Wearable skin-like strain sensors are becoming essential in diverse future applications, such as motion detection [1-11], soft robotics [12-15] and various biomedical applications [2,13-14,16-18]. As depicted in **Figure 1**, Among numerous nanomaterials and structures used to achieve novel flexible strain sensors, those based on carbon tend to exhibit greater mechanical performance [3,19-22] and gains unique potential of transparency [4,8,23-24], but also suffer from a low gauge factor (GF) and electrical conductivity. Similarly, sensors built with capacitive structures [10,11,23] demonstrate excellent linearity and low hysteresis but due to the theoretical limitations, also possess poor GFs (maximum of 1). Of this latter type, sensors based on silver nanowires (Ag NWs) [5,25-27] are suggested as the most promising candidate based on their excellent electrical and mechanical properties.
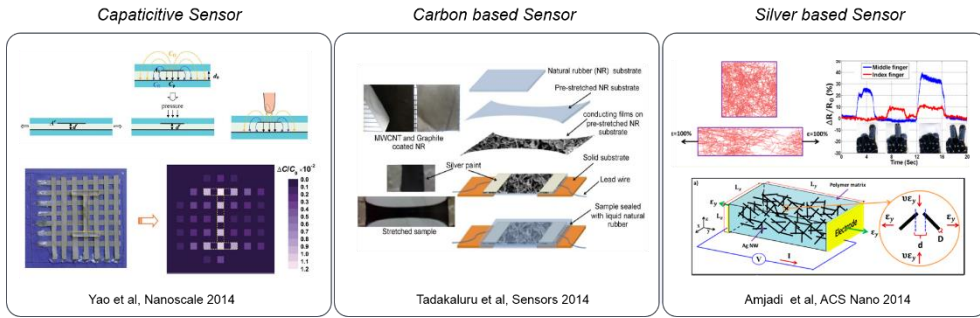
Figure 1 | Various types of strain/pressure sensors

However, in comparison to other recently reported silver-based strain sensors, they are only capable of detecting strain in a single direction. This hinders their application to detect more complex multi-axial, multi-dimensional strain conditions, with the only applicable uses being limited to areas on the body such as finger and

knee joints (i.e., single axial joints). These sensors have also limited research into the quantitative determination of complex conditions in various surface strain environments. In order to obtain relevant information under such conditions, sensors need the ability to detect strain in multi-dimensional directions so as to emulate the strain environment. However, it is difficult to make multi-dimensional strain sensors because they usually show strong coupled electrical conductance change in major axis of the principal strain and perpendicular direction due to Poisson's ratio. This problem becomes more severe under large strain condition and the conventional strain sensor needs to be exactly aligned with the principal strain to obtain accurate strain value.

1.2. Purpose of Research

To address the shortcomings of conventional single axis-strain sensor and to develop a novel scheme to detect random strain, this paper presents a highly stretchable and sensitive multi-dimensional strain sensor capable of detecting in real-time 'skin-like' multi-dimensional strain loadings using pre-strained Ag NW percolation networks. This relies on two pre-strained percolation network layers intersecting each other, with decoupled electrical resistance change to the major axis of the principal strain and perpendicular direction and thus independently detecting the x and y axis of the surface strain environment. This sensor is demonstrated to possess excellent performance (GF~20), large strain measurement (> 35%) and dynamic load performance with negligible hysteresis. Moreover, very long (>80 μm) nanowire arrays are used to allow an excellent mechanical and electrical stability in percolation network and uniform output signal. The response of the sensor was theoretically studied using 3D-percolation theory, which showed excellent correspondence with the experimental signals. Computational application of the sensor to the 3D model also allowed it to be successfully operated as a multi-axial controlling device. The amplitude and angle of strain was calculated from the signal obtained from the sensor in real-time, allowing the virtual 3D model to be controlled through finger movements. The proposed Ag NW network was also applied to 4×4 multi-pixel strain sensor array, fabricated by UV laser ablation, which allowed various strain conditions to be simultaneously monitored and modeled by surface strain distribution mapping.
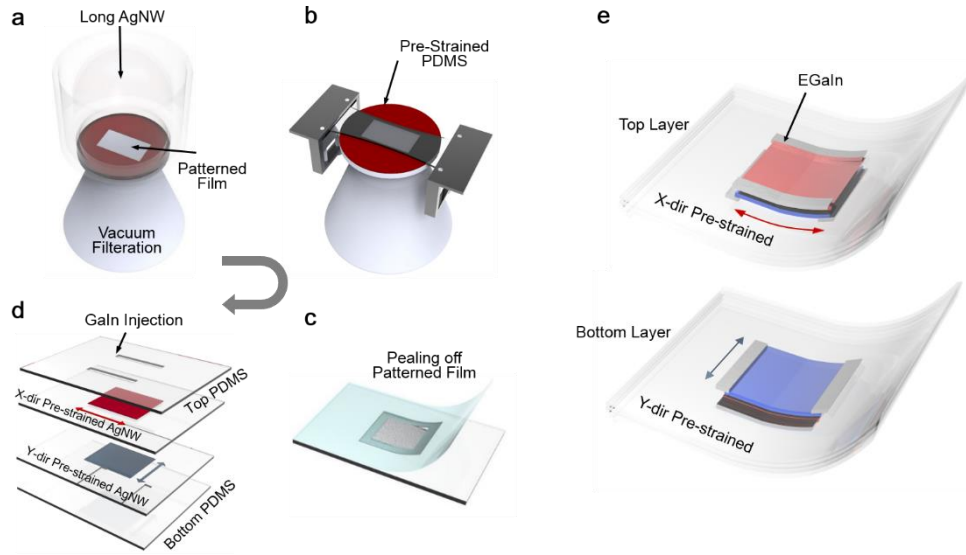
Chapter 2. Fabrication

2.1. Fabrication of the Strain Sensor

Multi-dimensional strain sensor composed of pre-strained Ag NW percolation network layers were prepared by vacuum filtration and transfer, as shown in **Figure 2a**. In this, a uniform percolation network film is first obtained by filtration of Ag NW solution, and then transferred to a pre-strained (100 %) PDMS substrate by applying uniform suction. The exterior of the Ag NW network is then detached and patterned by peeling off the adhesive film (**Figure 2a-2c**). Next, the patterned, pre-strained Ag NW film is encapsulated by a PDMS micro electrode channel layer with an uncured PDMS glue layer, the latter being designed to penetrate into the pore spaces between the Ag NW interconnections. After curing to attach the encapsulation layer, all of the Ag NWs become buried between the layers to form a sandwich structure. This tri-layer system is not only mechanically stable, but also resistant to surface buckling known to cause irreversibility of the resistance profile [5]. EGaIn is then injected into this micro channel to act as a stretchable liquid electrode, as this material offers a low viscosity at room temperature and a relatively high conductivity ($\sigma = 3.4 \times 10^4 S/cm$) [28, 29]. More importantly, it maintains its fluidity after injection, which is a critical factor in establishing electrical contact between the patterned Ag NW film and the electrode during deformation of the sensor. With the help of this liquid metal channel, the entire surface of the sensor can be deformed, allowing it to be used as a non-flat surface mountable device. Finally, two of these sandwich-structured assemblies were attached while intersecting each other (**Figure 2d**), with each functioning as single axis (*x* or *y*) strain sensors. The

structure of the resultant multiaxial sensor is shown in **Figure 2e**, which is composed of two individual pre-strained Ag NW strain sensors.

Figure 2 | Fabrication of a multidimensional strain sensor. (a) Vacuum filtration and transfer of very long Ag NW percolation networks. **(b)** Transferring process to the pre-strained PDMS substrate. **(c)** Edge patterning by detaching adhesive film. **(d)** Encapsulation of micro electrode channel and subsequent EGaIn injection. **(e)** Schematics showing two layers of the multi-dimensional strain sensor.

Optical photographs of a single pre-strained Ag NW strain sensor, two Ag NW sensors pre-strained at perpendicular directions, and final multidimensional strain sensor after interlocking are shown in **Figure 3a-3c**, respectively. Pre-strained AgNW films were prepared by pouring a 0.01 wt% AgNW solution dispersed in ethanol through a 0.2 μm porous membrane filter (diameter = 49 mm). Any ethanol remaining on the filter was gently dried by an air blower, after which the target pre-strained substrate (PDMS) was placed on top of the filter. A uniform vacuum pressure was applied to transfer the AgNW layer on to the target substrate, and then

the membrane was peeled off to leave the AgNW layer on the pre-strained substrate. This pre-strained substrate then steadily returned to its original non-strained condition.
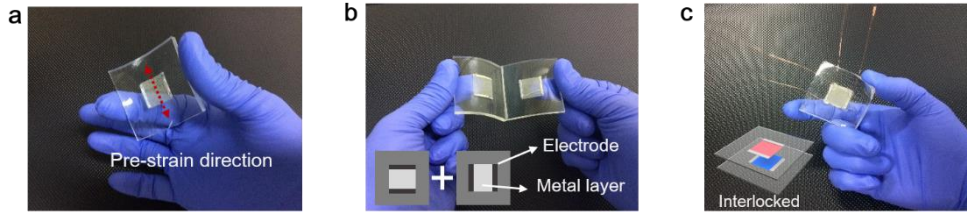
Figure 3 | Fabricated multidimensional strain sensor. (a) Single layer of the fabricated sensor. **(b)** Top and bottom layer before attaching. **(c)** Interlocked system of a multi-dimensional sensor with wire connection.

Patterns of micro electrode channels on the cover layer were defined by photolithography. PDMS (Dow corning, Sylgard 184) was poured on the wafer with SU-8 patterned master wafer and fully curing it in an oven at 100 ℃ for 20 mins. After peeling the cured PDMS from the wafer, channels measuring 250 μm in height were obtained (the fabrication of SU-8 master mold can be also replaced with the simple maskless fabrication. A PDMS glue layer was then spin coated onto the bottom of this cover layer and partially cured in an oven at 50 ℃ for 30 mins. Next, the partially cured cover layer was attached to the pre-strained AgNW film layer and fully cured in an oven at 100 ℃ for 10min. After injecting EGaIn (Aldrich) into the channel by applying a positive pressure with a syringe, a single copper wire was inserted into the EGaIn-filled micro electrode channel to transfer current and enable resistance measurement. The resulting channels therefore act as a stretchable and flexible electrode.
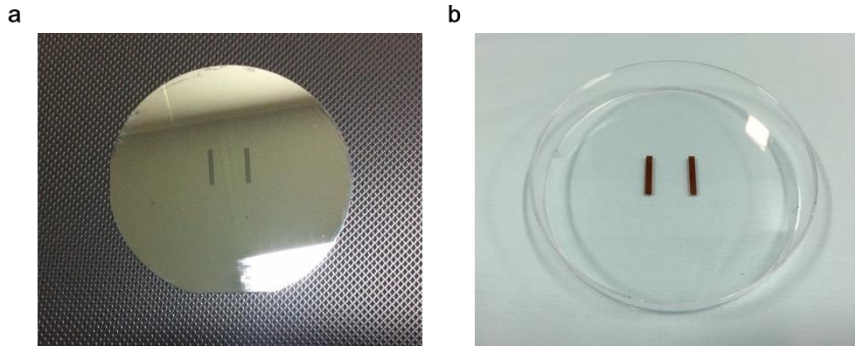
Figure 4 | Micro Electrode Mold (a) Micro electrode channel SU-8 mold on Si-wafer **(b)** Embossed PDMS mold made by Kapton tape (for the maskless simple fabrication of PDMS micro electrode channel)

2.2. Material

Modified polyol method was used to synthesize very long AgNWs. 0.234 g of PVP (Mw ~360,000) was added to 50ml of EG and dissolved by using a magnetic stir at 150 ℃. Afterward, a Cu-additive ($CuCl_2$) solution was dumped to PVP Solution. After 5~10 minutes, 15 ml of a 94 mM $AgNO_3$ solution were injected sequentially. The reaction condition was maintained until the synthesis was completed. The synthesized AgNWs were cleaned with acetone and ethanol at a 10:1 v/v ratio three times and collected by centrifugation of 3000 rpm for 20 mins. The SEM image of the synthesized silver nanowire is shown below.
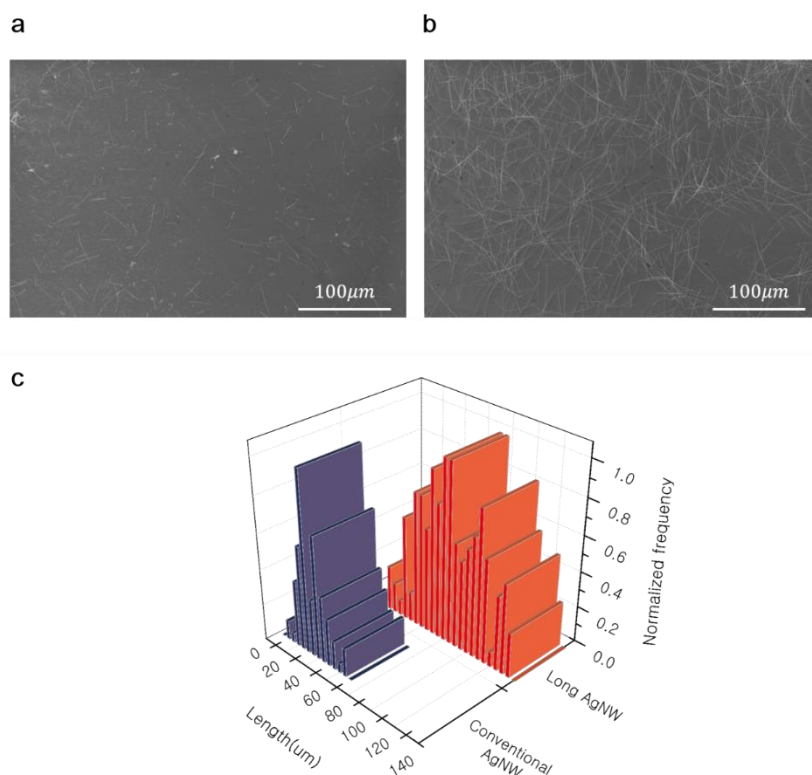
Figure 5 | Length characterization of the synthesized long Ag NWs (a) SEM image for conventional Ag NW **(b)** SEM image for long Ag NW **(c)** The length distribution of NWs

Chapter 3. Result

3.1. Pre-strained AgNW

The microscopic behavior of the surface of the pre-strained Ag NW film under 100 % applied strain in either the parallel (right column) or perpendicular (left column) direction with respect to the pre-strain direction (central column) is shown in **Figure 6a** SEM pictures. Note that as the PDMS substrate shrinks to its original size after Ag NW transfer process, the surface of the Ag NW film becomes corrugated. This pre-strained Ag NW percolation network film yields decoupled electrical conductance change in the applied mechanical strain direction and perpendicular direction, while the GF for conventional single axis strain sensors show highly coupled electrical conductance change due to Poisson's ratio. The physical phenomenon behind the polarized and decoupled resistance change in perpendicular direction and parallel direction (**Figure 6b**) can be explained by these surface conditions. The strain applied to the pre-strained direction (**Figure 6a**, right inset, 'parallel direction') caused the surface to become unwrinkled, yet still maintain its percolation network and electrical conductance until it reaches the pre-strain value. This made possible by the fact that Ag NWs are very ductile and malleable, and therefore capable of enduring a large degree of strain and deformation [30]. Since the corrugated surface is structurally flattened along the parallel to the pre-strain direction (**Figure 6a**, right inset, 'parallel direction'), a resistance shows almost no change up to certain strain. In contrast, the strain applied to the perpendicular to the pre-strain direction (**Figure 6a**, left inset, 'perpendicular direction') causes the distance between nanowires to increase, deforming them in the strain direction while maintaining their wavy surface in parallel direction. Since the Ag NWs used in this

study is much longer (>80 μm) than typical Ag nanowires (1-20 μm) [31], it is possible to make more effective use of the percolation network with greater stretchability [30] and stability of the resistance profile under the strain in any direction.
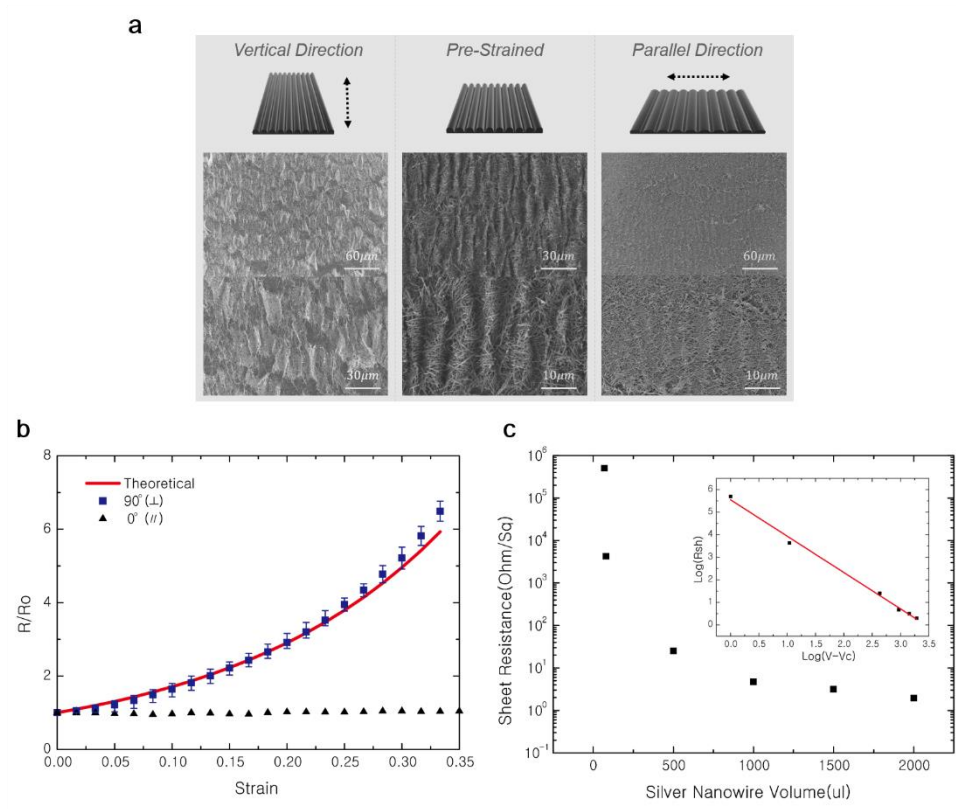
Figure 6 | Decoupled and polarized response of the Ag NW network strain sensor. (a) SEM image showing the surface of the sensor when strain is applied in the perpendicular (right column) and parallel direction (left column). **(b)** Variation in resistance for parallel (0°) and perpendicular (90°) directional deformation in comparison with the theoretical value derived by 3D percolation theory. **(c)** Sheet resistance as a function of the volume of silver nanowires. The inset shows a logarithmic plot of the data with a linear fit.

As shown in **Figure 6b**, a strain applied at 0° (triangle symbol, parallel to the pre-strained direction) generates almost no resistance variation, while a 90° strain (square symbol, perpendicular to the pre-strained direction) generates a dramatic increase in resistance. In other words, the proposed pre-strained strain sensor shows polarized and decoupled resistance change to a principal strain axis and therefore; displays a sinusoidal response to off-axis strain angles. As a result, the two crossing strain sensors are capable of independently detecting the transverse and longitudinal axes strain. This trend has been maintained at least up to 35% strain, while the limit of detection [32] towards the perpendicular direction is measured to be as small as 0.5%.

Physical analysis of the proposed Ag NW percolation network strain sensor was carried out using 3D percolation theory $\sigma = \sigma_0 (V - V_c)^\alpha$, where σ_0 is the electrical conductivity of the Ag NWs (630,000 S/cm), σ is the electrical conductivity of the Ag NW network, V is the volumetric fraction of Ag NWs in the filler (PDMS), V_c is the volumetric fraction of Ag NW at the percolation threshold, and α is the critical fitting exponent. **Figure 6c** shows the change in sheet resistance with nanowire volume, being measured by a four-point method after transferring the metal layer to the glass substrate. For the given nanowire concentration of 0.1 mg/ml (ethanol based) used in this study, the percolation threshold was calculated as a surface concentration of 7.276 µl/cm^2, the validity of which was confirmed through Monte-Carlo simulation (**Chapter 3.3**). This percolation threshold represents the minimum amount of Ag NWs required to ensure a successive percolation network to achieve a conductive film. The best fitting line was obtained by taking a value of a α =1.612, which corresponds to the inclination of the fitted line of the $log(R_{sh})$ vs $log(V\text{-}V_c)$ graph (**Figure 2c, inset**). As strain is applied, the volume of filler (V_{pdms})

is increased, while the volume of AgNW (V_{AgNW}) remains the same. Consequently, the volumetric fraction of V (V_{AgNW}/V_{pdms}) decreases with increasing strain, leading to a decrease in conductivity. Using these obtained values, the theoretical variation in resistivity was successfully calculated and found to match well with the experimental values given in **Figure 6b** (red line). Furthermore, the initial resistance of the strain sensor (5.3 Ω) increased significantly to 36 Ω, which is nearly seven times larger than the initial resistivity when a 35 % strain was applied.

3.2. Calculation of resistance through 3D percolation theory

The electrical conductivity of the g NW embedded PDMS composite is expressed by 3D percolation theory [33] as:

$$\sigma = \sigma_0 (V - V_c)^\alpha \tag{1}$$

The volumetric fraction of Ag NW can be expressed as:

$$\sigma_0 \left(\frac{V_{sil}}{V_0(1 + \varepsilon)(1 - \gamma\varepsilon)^2} - \frac{V_{silc}}{V_0} \right)^\alpha \tag{2}$$

$$= \sigma_0 (\frac{V_{sil}}{V_0})^\alpha \left(\frac{1}{(1 + \varepsilon)(1 - \gamma\varepsilon)^2} - \frac{V_{silc}}{V_{sil}} \right)^\alpha \tag{3}$$

where V_0 is the initial volume of PDMS, $V_{sil}(181.8\mu l/cm^2)$ is the volume of Ag NW, $V_{silc}(7.276\mu l/cm^2)$ is the volume of Ag NW at the percolation threshold, and ε is the tensile strain. If we define K as V_{silc}/V_{sil}, then the resistivity and initial resistivity of the composite under tensile strain can be determined by the following equations:

$$R = \rho \frac{L}{hw} \tag{4}$$

$$= \sigma_0 (\frac{V_{sil}}{V_0})^{\alpha^{-1}} \left(\frac{1}{(1 + \varepsilon)(1 - \gamma\varepsilon)^2} - K \right)^{-\alpha} \frac{l(1 + \varepsilon)}{h\,w(1 - v\varepsilon)^2} \tag{5}$$

$$R_o = \sigma_0 (\frac{V_{sil}}{V_0})^{\alpha^{-1}} (1 - K)^{-\alpha} \frac{l}{h\,w} \quad (when\ \varepsilon = 0) \tag{6}$$

Then the resistance ratio is expressed as:

$$\frac{R}{R_o} = \left(\frac{\frac{1}{(1+\varepsilon)(1-\gamma\varepsilon)^2} - K}{1 - K}\right)^{-\alpha} \frac{(1+\varepsilon)}{(1-\nu\varepsilon)^2} \qquad (7)$$

From this, the resistance ratio under strain can be calculated by inserting the experimental parameters ($K = 0.048$, $\alpha = 1.618$) into Eq. 7.

In order to define the initial resistance value, we first need to calculate Eq 6. Since the initial width (w) and length (l) are identical, a parameter for height (h) is needed to define Eq. 6. For this, the silver layer was partially removed over a width of 3μm using laser ablation. An AFM image showing a 10μm × 10μm sectional view of the boundary layer is given in **Figure S1**, from which the average height of the silver layer was calculated as 350nm. This AFM image was obtained using the SPA-400 scanning probe microscope installed at the National Center for Inter-university Research Facilities (NCIRF) at Seoul National University.
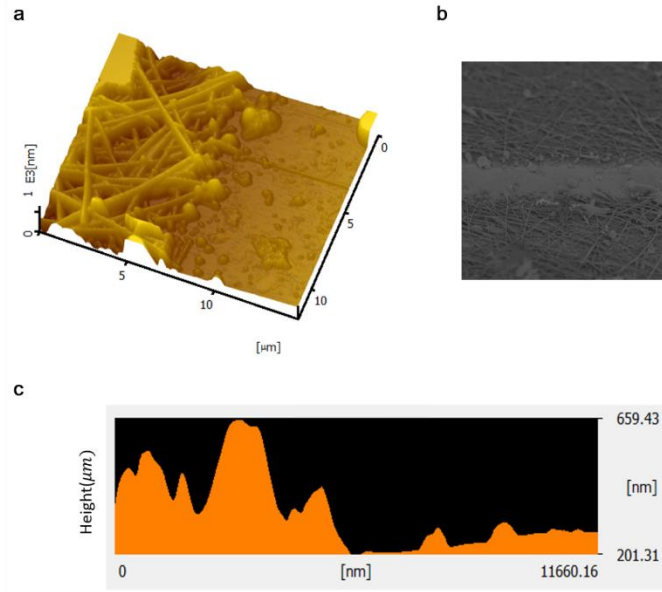
Figure 7 | Analyzing the height of the AgNW layer. (a) AFM image of the boundary layer (b) SEM image of laser ablated region   (c) Average height profile from AFM

3.3. Monte-Carlo simulation of resistance through 3D percolation theory

Monte Carlo simulation was used to validate the experimental value of V_{silc}. For this, a 2D simulation cell measuring 500μm × 500μm was first generated, in which 500 virtual lines of Ag NW were randomly distributed [34]. These lines had a fixed length of 80 μm (the average length of very long Ag NWs in **Figure S5**), with the percolation probability being determined from the formations of fully connected Ag NWs between the top 5 % and bottom 5 % of the silver layer. Percolation probability was averaged across 100 simulation runs for each segment.
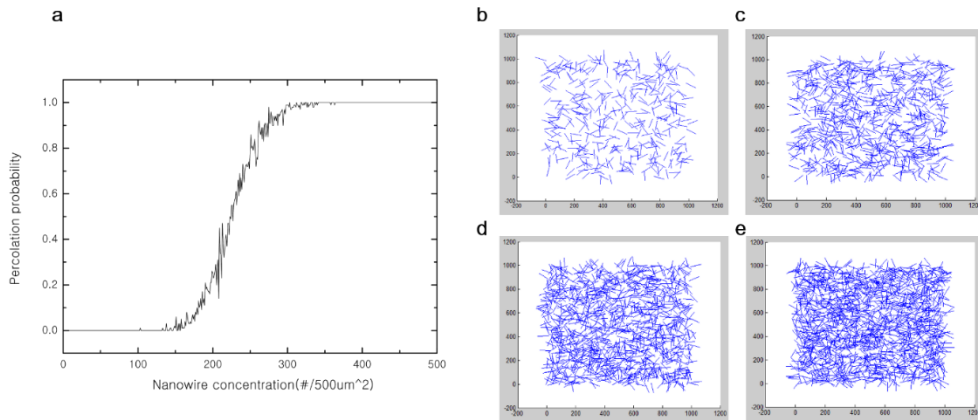
Figure 8 | Monte-Carlo simulation results. (a) Percolation probability versus nanowire concentration (b) Wire distribution at 100#/500 μm² (c) at 200#/500 μm² (d) at 300#/500 μm² (e) at 400#/500 μm²

The percolation point could be defined as that at which the percolation probability reaches 0.5, which from **Figure S4**, would appear to be around 250 nanowires per 500 μm²:

$$N(\#/cm^2) = \frac{4 \times d \times V}{\rho \times \pi \times D^2 \times L} \qquad (8)$$

where d is the concentration of the nanowire solution (0.1 mg/ml), V is the volume of the nanowire solution used per area, ρ is the density of silver (10.49 g/cm³), D is the diameter of the nanowires (100 nm) and L is the length of the nanowires (80 μm).

From Eq. 12, the volume of nanowires used could can be obtained from reference [35],

$$V(ul/cm^2) = \frac{\rho \times \pi \times D^2 \times L \times N}{4 \times d} \qquad (9)$$

By inserting the number of nanowires at the percolation point (250 nanowires per 500 μm²) into Eq. 13, the volume of nanowires at percolation is found to be 6.592 μl/cm², which matches well with the experimental value of 7.276 μl/cm².

In addition, the number concentration (#/area) of nanowires at percolation threshold computationally studied in the previous study [36] are defined as:

$$l\sqrt{\pi N_c} = 4.236 \qquad (10)$$

Substituting $l = 80\ \mu m$ gives $N_c = 223\ nanowires\ /\ 500\ \mu m^2$, which also well matches with the calculated value from Monte-Carlo simulation.

3.4. Off-axis strain detection of multi-dimensional strain sensor

In order to demonstrate the proposed sensor's ability to detect multi-dimensional strain, the results obtained by the experiment shown in **Figure 9** were compared with theoretical calculations (black lines in **Figure 9c-9e**). The resistance of the Ag NW percolation network film pre-strained in the *x*-direction (parallel to the pre-strained direction) is affected by the strain applied in the *y*-direction (perpendicular to the pre-strained direction). Therefore, if there is a strain δ applied in the off-axis direction (maximum principal strain direction, θ degree rotated from the pre-strained direction), the deformation affecting electrical conductivity will be $\delta \cdot sin^2\theta$. Owing to the inherent limitations of a single-axial tensile testing stage, applying a uniform axial strain in a specific off-axis direction is the most challenging technique in the aspects of theoretical and quantitative analysis. This problem was therefore approached by simply rotating the metal layer during the transfer process rather than vary the axial direction of strain, as depicted in **Figure 9b** (where the direction of strain is maintained along the *x*-axis). The effective strain (ES) factor in this case is determined as *cosθ/(1+tanθ)* (See **Chapter 3.4**), and makes it possible to calculate the effective strain by simply multiplying to the original strain value. This, in turn, allows the amplitude of the resistance to be predicted for various strain directions, as shown in **Figure 9c-9e** (blue triangles, 'projected from experiments'). A single Ag NW percolation network layered sensor was deformed in a tensile testing stage while measuring the minute resistance variation at 1.25 % strain intervals. As mentioned earlier, the response output of the sensor increases with off-axis angle (90°, perpendicular to the pre-strained direction), and by multiplying the ES factors at 60°,

45° and 30° (0.549, 0.353, 0.183 respectively) with their corresponding strain values, the effective strain is found to match perfectly with the original resistance profile at 90° strain angle deformation (black lines). This successfully demonstrates the accurate performance of the strain sensor, and from the information above, it is possible to calculate and predict the resistance responses on arbitrary strain directions and strain values. Moreover, one can inversely calculate both the magnitude of the maximum principal strain and its direction from the measured change in resistance by using two perpendicular strain sensors, as these independently detect the perpendicular axes of the maximum principal strain.
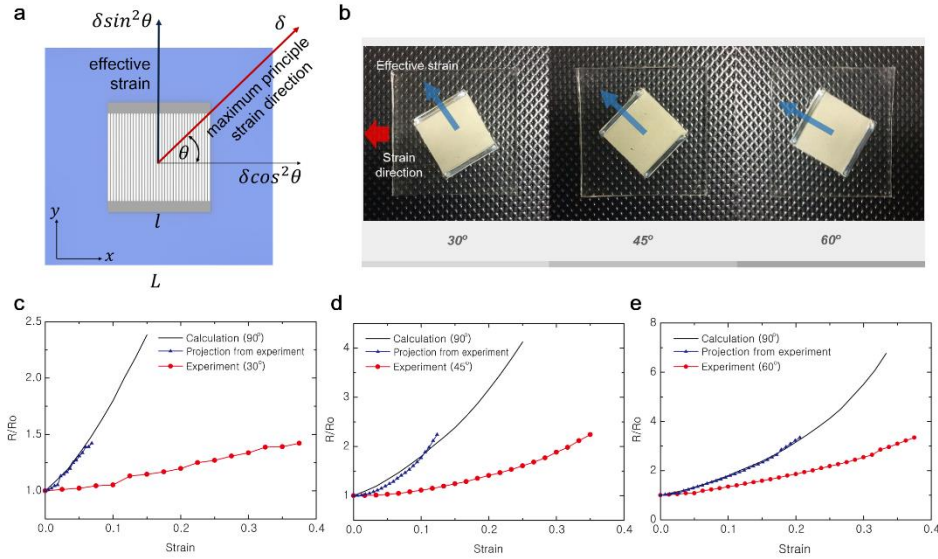
Figure 9 | Detecting off-axis principal strain. (a) Schematic of the strain components applied to the strain sensor. **(b)** Photographs of the metal layer rotated to different angles. **(c-e)** Comparison of the variation in resistance of the rotated sensor with that of the sensor strained at 90°. Blue triangle lines shows the projected strain value for 90° from experiment data for each off-axis rotation.

23

3.5. Calculation of the effective strain for off-axis deformation

Strain components of the rotated strain sensor used to calculate the effective strain on the sensor are illustrated in **Figure 10**. The rotated coordinates are defined as x^* and y^*. As mentioned in the main paper, the effective strain would be $\delta \cos^2\theta$ (x^* direction), which is perpendicular to the pre-strained direction.
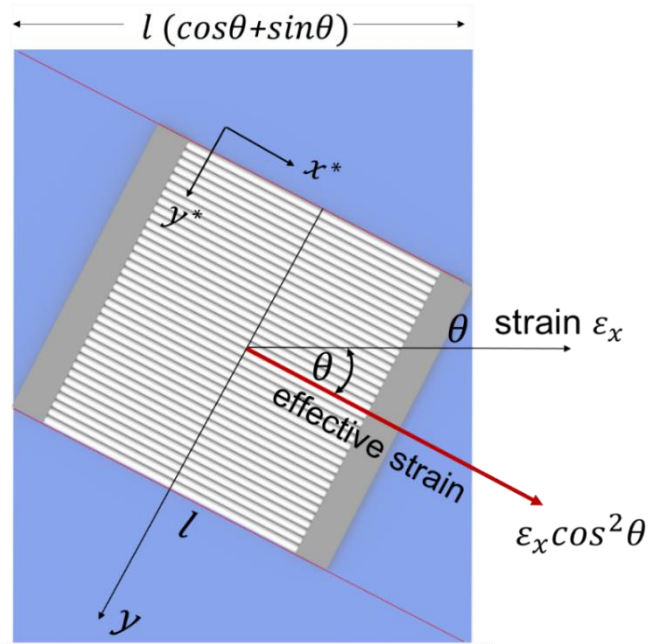
Figure 10 | Schematic of strain components applied on the rotated strain sensor.

When a strain ε_x is applied to the substrate as shown in **Figure 10**, the strain along x^* can be calculated from strain transformation as: [38]

$$\varepsilon_{x*} = \left(\frac{\varepsilon_x + \varepsilon_y}{2}\right) + \left(\frac{\varepsilon_x - \varepsilon_y}{2}\right) \cos 2\theta + \frac{\gamma_{xy}}{2} \sin 2\theta \qquad (11)$$

Since the strain is applied along x direction, $\varepsilon_y = \gamma_{xy} = 0$ and the equation is simplified as:

$$\varepsilon_{x*} = \varepsilon_x \cos^2 \theta \qquad (12)$$

Considering when the total amount of elongation along x axis is dx: $(\varepsilon_x \cdot L = dx)$

$$\varepsilon_{x*} = \frac{dx}{L} \cos^2 \theta = \frac{dx \cdot \cos^2 \theta}{l(\sin \theta + \cos \theta)}$$
$$= \frac{dx}{l} \cdot \left(\frac{\cos \theta}{1 + \tan \theta} \right) \qquad (13)$$

The effective strain factor (ES factor) would be therefore be:

$$\frac{\cos\theta}{1 + \tan\theta} \qquad (14)$$

3.6. Cyclic response of the strain sensor

The response of the strain sensor under cyclic strain (**Figure 11**) were recorded in various off-axis strain directions by applying minute manual deformation with fingers. The black line represents the x-axis pre-strained sensor, while the red line is the y-axis pre-strained sensor. As can be seen in the figure (**Figure 11**), an erratic movement of the finger was precisely and instantaneously recorded on the output signal. Under the off-axis strain at $0°$, the y-axis pre-strained sensor (red line) shows substantial response, while x-axis pre-strained sensor (black line) does not reacting to the strain signal. At $45°$, however, both x- and y- axis sensors show identical output signals, while at $90°$, the variation is opposite to that observed at $0°$.

The maximum principal strain (amplitude and direction of maximum principal strain) can be theoretically calculated using the schematic illustrated in **Figure 8a**. If we assume that there is a strain δ applied in the off-axis (θ) direction, then the strain on each axis can be expressed as $\delta_x = \delta \cos^2\theta$ and $\delta_y = \delta \sin^2\theta$ for the x-axis and y-axis, respectively. The strain direction of the sensor can be expressed as $\theta = tan^{-1}\sqrt{\delta y/\delta x}$, and the amplitude of the maximum principle strain can be further expressed as $\varepsilon = \delta_x/\cos^2\theta$ or either as $\varepsilon = \delta_y/\sin^2\theta$. Thus, the direction of the maximum principal strain can be easily calculated by analyzing the amplitude ratio of the two sensors' output. For example, with $45°$ strain applied, the ratio between δ_x and δ_y is one, which explains the identical strain variation observed. To measure the accuracy and response time of Ag NW percolation network strain sensor, a linear actuator system was used to apply dynamic cyclic strain (10%). The output signals recorded from the sensor are given in **Figure 12a**, and show excellent

agreement with the resistance profile theoretically calculated from **Figure 6b**. **Figure 12b** shows the long term reliability of the sensor. Signals collected after 1000 cycles showed that there is negligible change in the resistance profile with repeated loading.
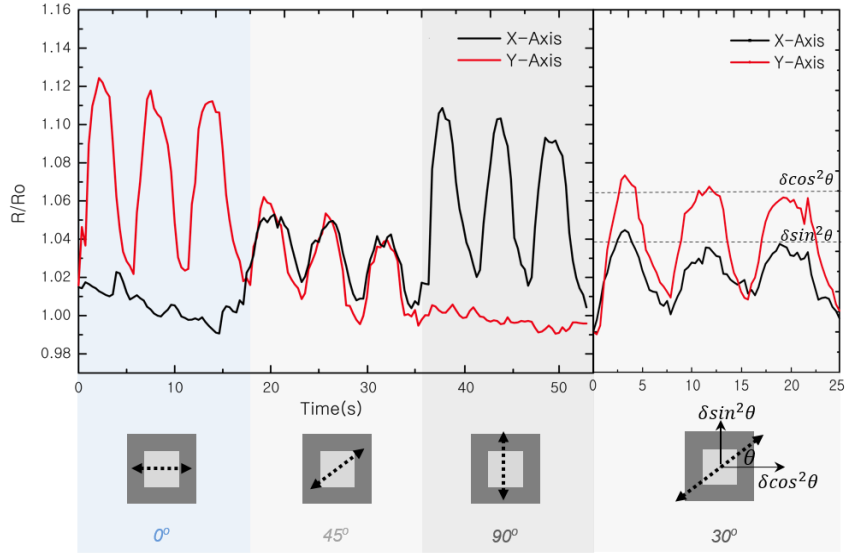
Figure 11 | Real-time monitoring of load-unload strain cycles at various off-axis strain angles (0°, 45°, 90°, 30°).
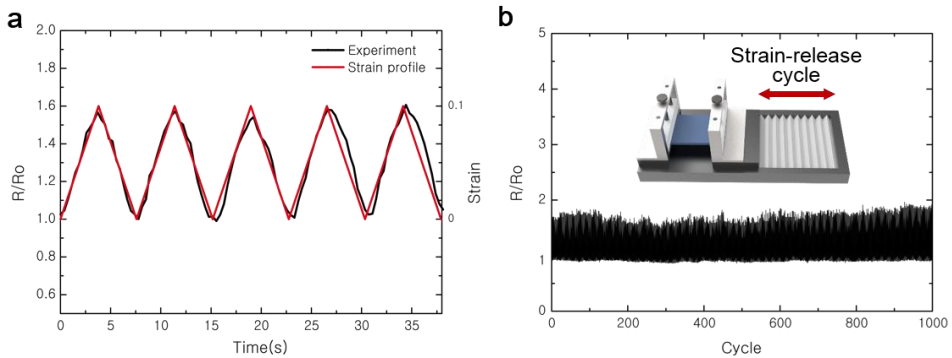
Figure 12 | Cyclic response of the proposed strain sensor. (a) Response of a strain sensor under the prescribed dynamic strain profile. **(b)** Long term cyclic strain response test (1000 cycles).

3.7. Multi-pixel strain sensor fabrication

To detect areal strain distribution, a (4×4 array) of 16 pixels of pre-strained silver nanowire network was fabricated by laser controlled ablation [37] (Nanio Air, INNOLAS Co.).
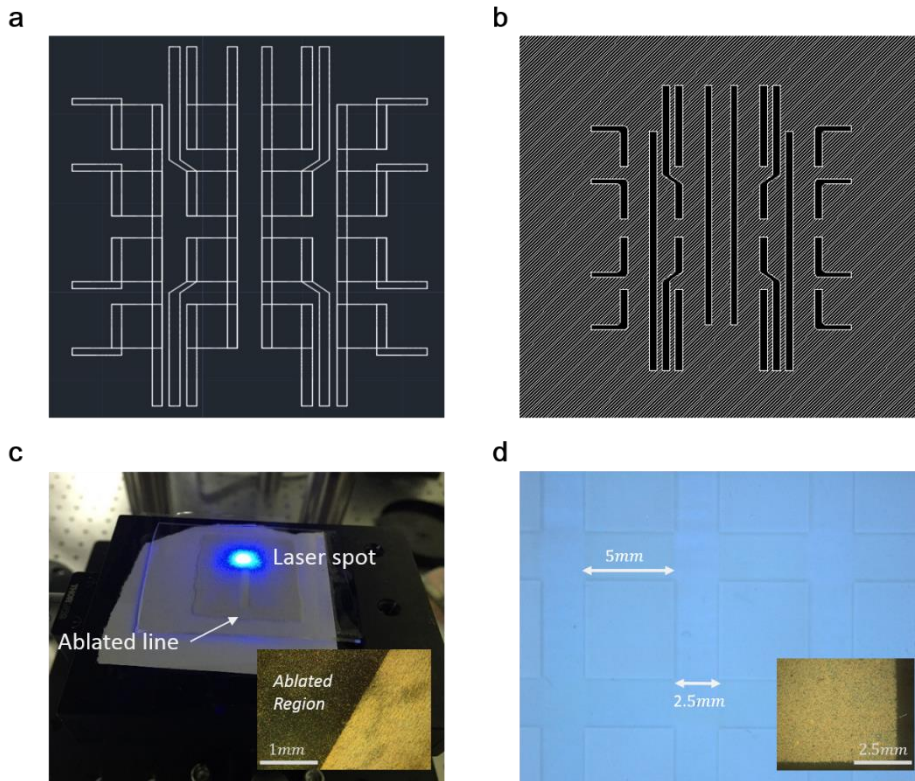
Figure 13 | Multi-pixel array fabrication by laser ablation. (a) CAD model for electrodes and multi-pixel arrays (b) CAD model for multi-pixel micro electrode channel (c) Photograph of process of laser ablation. The inset shows the microscopic image of ablated region of nanowire (d) Microscopic image of ablated metal layer region.

Each pixel was composed of a 5mm× 5mm metal layer island with 2.5mm intervals.

The laser properties were as shown below

| Laser Conditions |
| --- |
| *Pulse frequency : 30kHz* |
| *Diode operating current : 37A* |
| *Diode standby current : 8A* |
| *Laser amplitude : 30W* |

3.8. Applications of multi-dimensional strain sensor

The multi-dimensional strain sensors can be used as an input device of a maximum principal strain information. A virtual 3D simulation model of a multi-axis translation stages was connected to the multi-dimensional Ag NW percolation network strain sensor and its movement was controlled by the strain sensor signal with communication provided through a home-made data acquisition system linked to a 3D CAD program. This allowed the model to be successfully controlled by a finger in the 0°, 45° and 90° directions, as shown in **Figure 14a**.

Another advantage of Ag NW based strain sensor is that its patterning can be conducted very easily. Through simple patterning process, Ag NW percolation network enables spatial mapping of strain. A multi-pixel strain senor array of 16 (4×4) is fabricated by UV laser ablation patterning of the Ag NW percolation network for simultaneous measurement of the spatial strain distribution. As an application, strain distribution of the hand grip is monitored by the fabricated multi-pixel strain sensor. Human hand is a very complex organ capable of many different motions and fine motor skills. Therefore, it is extremely difficult to anticipate complete hand motion by simply measuring its 2D strain state. We hence concentrate on one of its representative motions - hand grip – which largely involves strain in y-direction. In this purpose, other strain, such as abduction and adduction in x-direction, affects the measurement as accumulating unwanted signals. Therefore, Ag NW percolation network pre-strained in x-direction has been used to exclude the strain components in x-direction which are irrelevant to our purpose. PDMS micro electrode array was subsequently encapsulated above the metal layer pixels with following process of EGaIn injection, as demonstrated in **Figure 14b**.
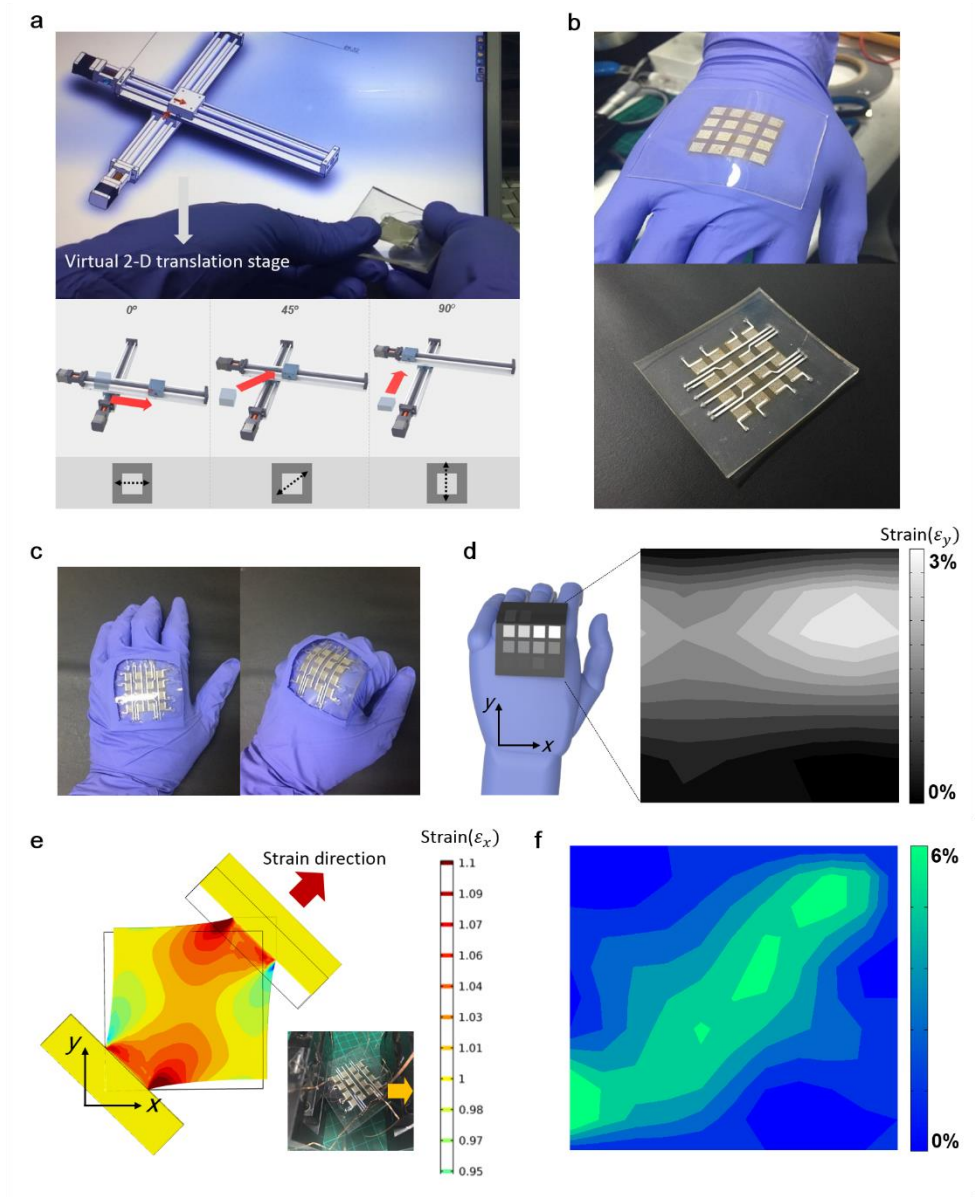
Figure 14 | Demonstration of applications of multi-dimensional strain sensors.
(a) Control of a virtual 3D translation stage using a multi-dimensional strain sensor.
(b) Photograph of a multi-pixel strain sensor array. (c) Photograph of the sensor
embedded in a glove to provide hand grip motion. (d) Mapping of the strain
distribution for hand grip motion in (c). (e) FEA simulation of 45° elongation and a
strain distribution of ε_x. (f) Experimental mapping of the ε_x   strain distribution

for random directions of strain loading. Experimental results show good agreement with FEA simulation in (e).

The photograph of the resultant sensor embedded in a glove for the measurement is provided in **Figure 14c**. In the strain distribution map provided in **Figure 14d**, the brighter spot corresponds to a region of greater elongation. It is noticeable that the maximum strain is detected at the joint as anticipated. To further explore the sensor's ability to detect random directional loadings, a 5 % strain was applied in the $45°$ direction to the multi-pixel strain sensor. The experimental settings were identical to those modeled in the finite element analysis (FEA) simulation (calculated strain distribution through FEA in the x-direction (ε_x) are shown in **Figure 14e**). As evidenced by the experimental results in strain mappings (**Figure 14f**), the sensor is perfectly capable of distinguishing and detecting strain distribution on the surface, showing excellent agreement with the strain distribution modeled by FEA simulation.

Chapter 4. Summary

In summary, we have presented a highly sensitive, flexible and stable multi-dimensional strain sensor that could be applied to next-generation multi-dimensional electronic sensing devices. This sensor consists of a pre-strained metal nanowire percolation network created through a simple fabrication method with the very long nanowires of which greatly enhance the electrical performance of the sensor. The proposed metal nanowire wire percolation network strain sensor showed highly polarized and decoupled electrical resistance change in the axial direction and perpendicular direction and could measure the maximum principal strain. Experimentally obtained properties of the resultant strain sensor in terms of large GF (~20) and large stretchability (35 %) show its potential to detect any kind of natural strain where a large strain and sensitivity are required. Furthermore, as the sensor is applicable to both 2-dimensional controlling devices and areal strain detection, it may have high impact in the implementation of future wearable device that often requires both monitoring and controlling of various surface conditions in human skin, mechanical structures and soft robotics.

References

1. Pang C, et al. A flexible and highly sensitive strain-gauge sensor using reversible interlocking of nanofibres. Nature materials 11, 795-801 (2012).
2. Park J, et al. Giant tunneling piezoresistance of composite elastomers with interlocked microdome arrays for ultrasensitive and multimodal electronic skins. ACS nano 8, 4689-4697 (2014).
3. Cohen DJ, Mitra D, Peterson K, Maharbiz MM. A highly elastic, capacitive strain gauge based on percolating nanotube networks. Nano letters 12, 1821-1825 (2012).
4. Cai L, et al. Super-stretchable, transparent carbon nanotube-based capacitive strain sensors for human motion detection. Scientific reports 3, 3048 (2013).
5. Amjadi M, Pichitpajongkit A, Lee S, Ryu S, Park I. Highly stretchable and sensitive strain sensor based on silver nanowire–elastomer nanocomposite. ACS nano 8, 5154-5163 (2014).
6. Lessing J, Morin SA, Keplinger C, Tayi AS, Whitesides GM. Stretchable Conductive Composites Based on Metal Wools for Use as Electrical Vias in Soft Devices. Advanced Functional Materials, n/a-n/a (2015).
7. Li X, et al. Stretchable and highly sensitive graphene-on-polymer strain sensors. Scientific reports 2, 870 (2012).
8. Lipomi DJ, et al. Skin-like pressure and strain sensors based on transparent elastic films of carbon nanotubes. Nature nanotechnology 6, 788-792 (2011).
9. Muth JT, et al. Embedded 3D printing of strain sensors within highly stretchable elastomers. Advanced materials 26, 6307-6312 (2014).
10. Viry L, et al. Flexible three-axial force sensor for soft and highly sensitive artificial touch. Advanced materials 26, 2659-2664, 2614 (2014).
11. Woo S-J, Kong J-H, Kim D-G, Kim J-M. A thin all-elastomeric capacitive pressure sensor array based on micro-contact printed elastic conductors. Journal of Materials Chemistry C 2, 4415 (2014).
12. Ma R, Lee J, Choi D, Moon H, Baik S. Knitted fabrics made from highly conductive stretchable fibers. Nano letters 14, 1944-1951 (2014).
13. Kim J, et al. Stretchable silicon nanoribbon electronics for skin prosthesis. Nature communications 5, 5747 (2014).
14. Lu N, Lu C, Yang S, Rogers J. Highly Sensitive Skin-Mountable Strain Gauges Based Entirely on Elastomers. Advanced Functional Materials 22, 4044-4050 (2012).
15. Cheng M, Huang X, Ma C, Yang Y. A flexible capacitive tactile sensing array with floating electrodes. Journal of Micromechanics and Microengineering 19, 115001 (2009).

16. Huang X, et al. Materials and Designs for Wireless Epidermal Sensors of Hydration and Strain. Advanced Functional Materials 24, 3846-3854 (2014).
17. Kang D, et al. Ultrasensitive mechanical crack-based sensor inspired by the spider sensory system. Nature 516, 222-226 (2014).

18. Pang C, et al. Highly skin-conformal microhairy sensor for pulse signal amplification. Advanced materials 27, 634-640 (2015).

19. Alamusi, Hu N, Fukunaga H, Atobe S, Liu Y, Li J. Piezoresistive strain sensors made from carbon nanotubes based polymer nanocomposites. Sensors 11, 10691-10723 (2011).

20. Hu N, et al. Investigation on sensitivity of a polymer/carbon nanotube composite strain sensor. Carbon 48, 680-687 (2010).

21. Yamada T, et al. A stretchable carbon nanotube strain sensor for human-motion detection. Nature nanotechnology 6, 296-301 (2011).

22. Kang I, Schulz MJ, Kim JH, Shanov V, Shi D. A carbon nanotube strain sensor for structural health monitoring. Smart materials and structures 15, 737 (2006).

23. Wang X, Li T, Adams J, Yang J. Transparent, stretchable, carbon-nanotube-inlaid conductors enabled by standard replication technology for capacitive pressure, strain and touch sensors. Journal of Materials Chemistry A 1, 3580 (2013).

24. Bae S-H, Lee Y, Sharma BK, Lee H-J, Kim J-H, Ahn J-H. Graphene-based transparent strain sensor. Carbon 51, 236-242 (2013).

25. Yao S, Zhu Y. Wearable multifunctional sensors using printed stretchable conductors made of silver nanowires. Nanoscale 6, 2345-2352 (2014).

26. Xu F, Zhu Y. Highly conductive and stretchable silver nanowire conductors. Advanced materials 24, 5117-5122 (2012).

27. Yun S, Niu X, Yu Z, Hu W, Brochu P, Pei Q. Compliant Silver Nanowire-Polymer Composite Electrodes for Bistable Large Strain Actuation. Advanced materials 24, 1321-1327 (2012).

28. Dickey MD, Chiechi RC, Larsen RJ, Weiss EA, Weitz DA, Whitesides GM. Eutectic Gallium-Indium (EGaIn): A Liquid Metal Alloy for the Formation of Stable Structures in Microchannels at Room Temperature. Advanced Functional Materials 18, 1097-1104 (2008).

29. Kubo M, et al. Stretchable microfluidic radiofrequency antennas. Advanced materials 22, 2749-2752 (2010).

30. Lee P, et al. Highly stretchable and highly conductive metal electrode by very long metal nanowire percolation network. Advanced materials 24, 3326-3332 (2012).

31. Kumar A, Zhou C. The race to replace tin-doped indium oxide: which material will win? ACS nano 4, 11-14 (2010).

32. Currie, L.A. Limits for qualitative detection and quantitative determination. Application to radiochemistry. Analytical Chemistry 40, 586-593 (1968).

33. Aharony A, Stauffer D. Introduction to percolation theory. Taylor & Francis (2003).

34. Grujicic M, Cao G, Roy W. A computational analysis of the percolation threshold and the electrical conductivity of carbon nanotubes filled polymeric materials. Journal of materials science 39, 4441-4449 (2004).

35. Madaria AR, Kumar A, Ishikawa FN, Zhou C. Uniform, highly conductive, and patterned transparent films of a percolating silver nanowire network on rigid and flexible substrates using a dry transfer technique. Nano Research 3, 564-573 (2010).

36. Pike G, Seager C. Percolation and conductivity: A computer study. I. Physical review B 10, 1421 (1974).

37.   Hong S, et al. Nonvacuum, maskless fabrication of a flexible metal grid transparent conductor by low-temperature selective laser sintering of nanoparticle ink. ACS nano 7, 5024-5031 (2013).

38.   A. Ugural, "Mechanics of materials, 1991," ed: McGraw Hill, New York.

국문 초록

Highly Sensitive and Stretchable Multi-dimensional Strain Sensor with Pre-strained Anisotropic Metal Nanowire Percolation Networks

김권규 (Kyun Kyu Kim)
기계항공공학부 기계공학전공 (Mechanical Engineering)
Seoul National University

유연성을 가지면서 변형을 감지할 수 있는 스트레인 센서는 동작 감지 분야, 로봇 분야, 다양한 생물 의학 응용 분야 등 다양한 분야에서 활용될 수 있다. 특히, 인공피부의 경우, 다양한 사람의 동작 및 외부의 자극에 따른 피부의 변형을 민감하게 감지할 수 있어야 하며, 부드럽고 곡률을 가는 부위에 적용할 수 있어야 하며, 상당한 유연성 및 내구성을 필요로 한다. 또한, 사람의 동작 및 외부의 자극이 갖는 방향성을 감지할 수 있어야 한다. 최근 다양한 스트레인 센서에 관한 연구들이 발표되고 있으나 다차원적인 변형을 감지하는 데에 어려움이 있었다. 본 연구에서는 일차원 센서의 단점들을 극복하기 위하여 미리 인장된 은 나노와이어 퍼콜레이션 네트워크를 이용하여 가로와 세로 인장에 대한 분리된 신호를 얻어내는 데에 성공하였다. 35%의 높은 인장률과 게이지 펙터(>20)를 보이며 3D 퍼콜레이션 이론을 이용하여 이론적인 검증도 완료하였다. 더 나아가 넓은 면적의 센서 제작을 통하여 손에 부착할 수 있는 센서를 제작하였으며, 3D 가상 모델을 컨트롤 하는 체계를 구축하였다

Keyword : 다차원 스트레인 센서, 나노와이어 퍼콜레이션 네트워크, 유연전자소자, 이방성 저항 변화

Student Number : 2014-20654